

Exact complex-wave reconstruction in digital holography

Chandra Sekhar Seelamantula,^{1,*} Nicolas Pavillon,^{2,4} Christian Depeursinge,^{2,5} and Michael Unser^{3,6}

¹*Department of Electrical Engineering, Indian Institute of Science, Bangalore - 560012, India*

²*Advanced Photonics Laboratory, Ecole polytechnique fédérale de Lausanne (EPFL),
Station 17, CH-1015, Lausanne, Switzerland*

³*Biomedical Imaging Group, Ecole polytechnique fédérale de Lausanne (EPFL),
Station 17, CH-1015, Lausanne, Switzerland*

⁴*E-mail: nicolas.pavillon@epfl.ch*

⁵*E-mail: christian.depeursinge@epfl.ch*

⁶*E-mail: michael.unser@epfl.ch*

**Corresponding author: chandra.sekhar@ieee.org*

Received August 18, 2010; revised January 22, 2011; accepted February 18, 2011;
posted March 8, 2011 (Doc. ID 133630); published May 9, 2011

We address the problem of exact complex-wave reconstruction in digital holography. We show that, by confining the object-wave modulation to one quadrant of the frequency domain, and by maintaining a reference-wave intensity higher than that of the object, one can achieve exact complex-wave reconstruction in the absence of noise. A feature of the proposed technique is that the zero-order artifact, which is commonly encountered in hologram reconstruction, can be completely suppressed in the absence of noise. The technique is noniterative and nonlinear. We also establish a connection between the reconstruction technique and homomorphic signal processing, which enables an interpretation of the technique from the perspective of deconvolution. Another key contribution of this paper is a direct link between the reconstruction technique and the two-dimensional Hilbert transform formalism proposed by Hahn. We show that this connection leads to explicit Hilbert transform relations between the magnitude and phase of the complex wave encoded in the hologram. We also provide results on simulated as well as experimental data to validate the accuracy of the reconstruction technique. © 2011 Optical Society of America

OCIS codes: 090.1995, 100.2000, 100.3010, 100.3175, 120.5050, 180.3170.

1. INTRODUCTION

Digital holography is an efficient interferometric modality suitable for imaging the three-dimensional (3D) structure of specimens. Using this technique, one can reconstruct both the amplitude and the phase of a wavefront [1–3]. Its primary application areas are microscopy, nondestructive testing, profilometry, and so on [4–10]. The feature that distinguishes digital holography from traditional holography is the method of acquisition. In digital holography, the acquisition is done by a charge-coupled device camera and the reconstruction is performed numerically. The efficacy of standard digital holographic reconstruction is limited by two artifacts, namely, the conjugate/twin image and the zero-order. The zero-order leads to blurring of the desired image. Since the measurements are intensities, the twin image cannot be eliminated unless one resorts to phase-shifting techniques [11,12]. One solution to separating these components was proposed by Leith and Upatnieks [13], who recorded holograms in the off-axis geometry. The advantage of this configuration is that the zero-order, the desired image, and the twin image are physically separated from one another. The object wave can then be approximately recovered by using a band-pass filter [14,15], or a high-pass filter [16]. This approach is known as spatial filtering and relies on the critical assumption that the zero-order and desired diffraction orders are well separated so that the zero-order can be suppressed by filtering. The basic idea of separating the three diffraction orders by employing an off-axis configuration is remarkable; the downside, however, lies

in two aspects: (i) effectively, only a fraction of the available hologram spectrum is used for encoding the object wave; therefore, this scheme is not efficient at utilizing the spectral resource; and (ii) spatial filtering often requires manual intervention for selecting the desired order. Ideally, one would like to take maximum advantage of the available spectrum without distorting the object wave, without manual intervention, and without having to deploy sophisticated acquisition/reconstruction techniques.

Recently, we introduced a new nonlinear reconstruction technique [17,18], which enables exact zero-order-free reconstruction in off-axis holography configuration even if the zero-order and the object-wave spectra overlap. This is in contrast to spatial filtering methods [14–16], which require a clear separation between the zero-order and desired diffraction orders. The nonlinear technique works under two realistic assumptions on the recorded signal: (i) the spectrum of the object wave should be confined to a quadrant of the Fourier domain, and (ii) the intensity of the object wave should be smaller than that of the reference. The goal in [18] is primarily the experimental validation of the reconstruction technique, robustness to deviations in experimental conditions from the theoretical assumptions, and experimental assessment of phase stability. In this paper, we focus exclusively on the mathematical aspects underlying the technique and associated signal processing connotations. The contributions of this paper are as follows:

- A systematic and complete development of the mathematical components of the nonlinear reconstruction technique.

- A relationship between the nonlinear reconstruction technique and homomorphic signal processing: by recognizing the zero-order as a convolutional term in the frequency domain, we interpret our reconstruction technique as an exact deconvolution technique. This link implies that while the cepstrum, which is a homomorphic signal processing technique, fits in naturally to solve the deconvolution problem, other deconvolution techniques may also be developed to suppress the zero-order.

- A Hilbert transform formalism for analyzing the reconstruction technique: specifically, we show how particular forms of the Hilbert transform in two dimensions, namely, the *partial* and *total* Hilbert transforms, play a role in reconstruction.

- Explicit Hilbert transform relations between the measured hologram intensity and the phase of the underlying complex wave. These relations show that the technique recovers the phase starting from the intensity holograms. The proposed technique is new and is aimed at solving a particular type of phase-retrieval problem, which arises naturally in the context of holography, and is quite different from the type of phase-retrieval techniques proposed in [19]. More specifically, our technique is noniterative and exact whereas the techniques proposed in [19] are iterative and give rise to an approximate solution. To the best of our knowledge, such exact results and magnitude-phase relations have not been reported in the context of digital holography.

- Evaluation on simulated as well as experimental data to establish the accuracy of the technique, and comparisons with the standard Fourier filtering approach used in holographic reconstruction.

A. Organization of the Paper

In Section 2, we recall some preliminary ideas about hologram recording, classical reconstruction, and its discrete implementation. We also highlight the limitations of the conventional reconstruction. In Section 3, we develop the new reconstruction technique. The link between the proposed reconstruction technique and homomorphic signal processing is established in Section 4. We also report simulation as well as experimental results to validate the reconstruction technique (Section 5). The Hilbert transform relations are established in Section 6. The digital holographic microscopy setup assumed in this paper is defocused imaging in the off-axis configuration. However, the reconstruction technique and the conclusions drawn are also applicable to other off-axis configurations such as in-focus holography and Fourier holography.

2. PRELIMINARIES

A. Notations

We shall work mainly with two-dimensional (2D) functions that are defined either in space (argument: $\mathbf{x} = (x, y)$) or in frequency (argument: $\boldsymbol{\omega} = (\omega_x, \omega_y)$). The Fourier transform operator is denoted by \mathcal{F} . Its definition in 1D or 2D applies depending on whether its argument is a 1D function or a 2D function, respectively. The wave-vector is $\mathbf{k} = (k_x, k_y)$, where k_x and k_y are the wavenumbers in the x and y directions, respectively. The inner product of two index vectors is defined

in the usual sense and is denoted as $\langle \cdot, \cdot \rangle$; for example, $\langle \mathbf{k}, \mathbf{x} \rangle = k_x x + k_y y$. The inner product of functions is defined in the L_2 sense. Two-dimensional sequences are represented with the square bracket notation; for example, $\psi_i[\mathbf{m}]$ where the argument is $\mathbf{m} = [m, n]$ (spatial index); $\mathbf{p} = [k, \ell]$ (frequency index). The discrete Fourier transform operator is denoted by \mathcal{F}_d . The indicator function is defined as $\mathbf{1}_Q = 1$ over region $Q \subset \mathbb{R} \times \mathbb{R}$, and 0 elsewhere.

B. Off-Axis Hologram Recording

A hologram is formed as a result of the interference between two mutually coherent waves—one emanating from the object, denoted by $o(\mathbf{x})$, and the other a reference wave $r(\mathbf{x})$. The interference pattern has a spatial intensity distribution $i(\mathbf{x})$ given by

$$i(\mathbf{x}) = |r(\mathbf{x}) + o(\mathbf{x})|^2 \\ = |r(\mathbf{x})|^2 + |o(\mathbf{x})|^2 + r^*(\mathbf{x})o(\mathbf{x}) + r(\mathbf{x})o^*(\mathbf{x}). \quad (1)$$

The first two terms on the right-hand side of (1) correspond to the intensities of the reference and object waves, respectively. The intensity distribution $i(\mathbf{x})$ is referred to as the hologram. In classical holography, a photographic plate is used to record $i(\mathbf{x})$. In state-of-the-art digital holography systems [11,20], a digital acquisition device such as a charge-coupled-device (CCD) camera placed at the hologram plane captures the spatial intensity distribution. In the in-line configuration, the reference and object waves are parallel to one another. In off-axis holography, the two waves are separated by an angle θ , as shown in Fig. 1.

C. Hologram Reconstruction

Let us assume that the reference is a plane wave of spatially constant intensity $i_r = |r(\mathbf{x})|^2$. Let the intensity of the object wave be denoted by $i_o(\mathbf{x})$; i.e., $i_o(\mathbf{x}) = |o(\mathbf{x})|^2$. To reconstruct the hologram, a plane wave $u(\mathbf{x})$ is first used to illuminate the hologram. The wave $u(\mathbf{x})$ is therefore sometimes referred to as the *illumination wave*. This creates a field $\psi_o(\mathbf{x})$ given as

$$\psi_o(\mathbf{x}) = u(\mathbf{x})i(\mathbf{x}) \\ = \underbrace{i_r u(\mathbf{x}) + u(\mathbf{x})i_o(\mathbf{x})}_{\text{zero-order terms}} + \underbrace{u(\mathbf{x})r^*(\mathbf{x})o(\mathbf{x})}_{\text{virtual image}} + \underbrace{u(\mathbf{x})r(\mathbf{x})o^*(\mathbf{x})}_{\text{real image}}. \quad (2)$$

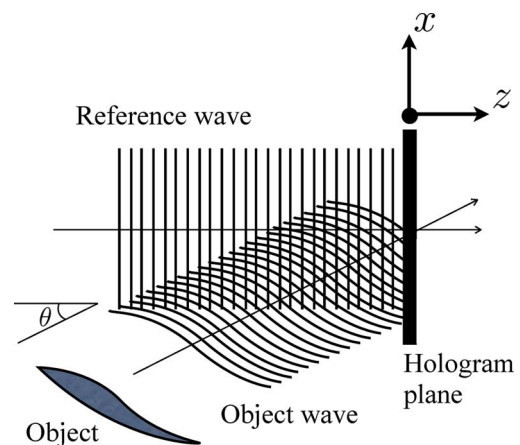


Fig. 1. (Color online) Off-axis digital holography—recording.

The zero-order terms comprise the plane wave $i_r u(x)$ and the object wave $u(x)i_o(x)$, whose spatial variation is a function of the object. Since the reference and object-wave intensities modify the amplitude but not the phase of $u(x)$, the zero-order terms propagate parallel to $u(x)$. The spatial spread of the zero-order depends on the spectrum of the object wave. The real image propagates at an angle $-\theta$ with respect to the illumination wave [the minus sign is a consequence of the complex-conjugation in (2)]. The virtual image is a reflection of the real image with respect to the hologram plane [cf. Fig. 2]. The physical separation between the three images is precisely the advantage of off-axis holography. The spatial locations of the three terms are shown in Fig. 2. For the special case where $u(x) = r(x)$, the real and virtual images are merely scaled by the intensity of the reference wave. When the distance of propagation equals the optical path distance d between the object and the hologram plane in the recording process, the real image comes into focus. In the opposite direction, at a distance equal to $-d$, the virtual image comes into focus. Thus, the real and virtual images are in general out of focus, but one of them can be brought into focus by appropriately adjusting the reconstruction distance.

D. Digital Hologram Reconstruction

By employing the Fresnel approximation [1,21], the underlying scalar diffraction pattern can be specified up to second-order accuracy. In practice, it is quite feasible to stay within the limits of this approximation. In this framework, we have the following expression for the reconstructed wavefront:

$$\begin{aligned} \psi_i(\xi) &= A \exp\left(\frac{i\pi}{\lambda d}(\xi^2 + \eta^2)\right) \int \psi_o(x) \exp\left(\frac{i\pi}{\lambda d}(x^2 + y^2)\right) \\ &\quad \times \exp\left(\frac{i2\pi}{\lambda d}(x\xi + y\eta)\right) dx \\ &= A \exp\left(\frac{i\pi}{\lambda d}(\xi^2 + \eta^2)\right) \\ &\quad \times \mathcal{F}^{-1}\left\{\psi_o(x) \exp\left(\frac{i\pi}{\lambda d}(x^2 + y^2)\right)\right\}, \end{aligned} \tag{3}$$

where λ is the wavelength and A equals the complex constant $B \frac{\exp(i2\pi d/\lambda)}{i\lambda d}$, B denoting a real scaling factor. The reconstruction plane corresponds to $x = \xi$ and $y = \eta$. The reconstructed wavefront is complex-valued and can be decomposed into two parts—modulus and phase, which are referred to as the amplitude- and phase-contrast images, respectively.

In digital Fresnel holography, the illumination wave is replaced by a digitally reproduced version of the physical

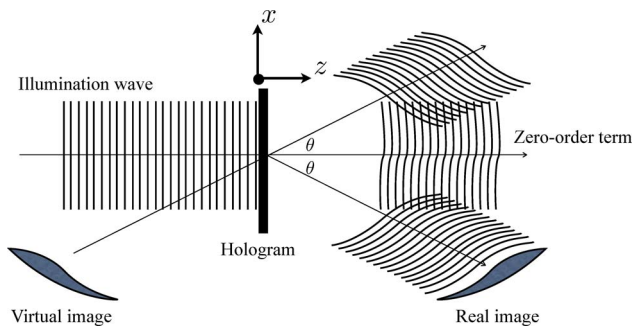


Fig. 2. (Color online) Off-axis digital holography—reconstruction.

reference wave used in the recording process. The physical propagation of the illuminated wave is simulated numerically by employing the Fresnel approximation. Therefore, in practice, one can only compute a discrete version of the integral in (3); the continuous-domain Fourier transform operator is replaced by the discrete Fourier transform (DFT) and the Fresnel approximation is computed efficiently by employing fast Fourier transform algorithms. In the discrete domain, the wavefront is given by

$$\begin{aligned} \psi_i[m] &= A \exp\left(\frac{i\pi}{\lambda d}(m^T \Delta_1 m)\right) \\ &\quad \cdot \mathcal{F}_p\left\{\psi_o[p] \exp\left(\frac{i\pi}{\lambda d}(p^T \Delta_2 p)\right)\right\}[m], \end{aligned}$$

where $\Delta_1 = \begin{pmatrix} \Delta\xi & 0 \\ 0 & \Delta\eta \end{pmatrix}$ and $\Delta_2 = \begin{pmatrix} \Delta x & 0 \\ 0 & \Delta y \end{pmatrix}$. The symbol

Δ associated with a variable denotes the corresponding sampling period; for example $\Delta\xi$ is the sampling period along the ξ axis. $\mathbb{F}\{\cdot\}_p$ denotes that the DFT operator acts along p . The 2D sequence $\psi_o[p]$ is the digital hologram obtained by spatial sampling of $\psi_o(x)$ at the detector:

$$\psi_i[m] = \psi_o(x) \cdot \mathbf{1}_{\left[0, \frac{x}{L_x}\right] \times \left[0, \frac{y}{L_y}\right]} \Big|_{x=(m\Delta x, n\Delta y)},$$

where L_x and L_y are the dimensions of the detector along the x and y axes, respectively; $\mathbf{1}_{\left[0, \frac{x}{L_x}\right] \times \left[0, \frac{y}{L_y}\right]}$ is the indicator function for the detector area; the symbol \times is used to denote the tensor product over intervals. It is common to employ detectors with square geometry, in which case we have $N_x = N_y = N$, $-\frac{N}{2} \leq k, \ell, m, n \leq \frac{N}{2}$; $L_x = L_y = L$; $\Delta x = \Delta y = \frac{L}{N}$. The sampling intervals along the spatial frequency variables ξ and η are given as $\Delta\xi = \Delta\eta = \frac{\lambda d}{L}$.

E. Problems in Conventional Reconstruction

The real image, the virtual image, and the zero-order terms overlap spatially. Another practical limitation is imposed by the finite size of the CCD plane, which always results in holograms of finite size. Moreover, within the discrete framework, we have access to the sampled version of the hologram. Sampling in the hologram plane inherently introduces periodicity in the reciprocal domain. The period is equal to the spatial support of the hologram, and within this region, the real, virtual, and zero-order images have to be accommodated. The support of the zero-order image along each axis is twice that of the real/virtual images. The virtual image is redundant and does not carry more information than the real image. Thus, the useful area is effectively reduced to a small percentage of the hologram area (for example, the value is 6.25% for the spectral diagrams shown in Fig. 3). It would be highly desirable to increase the usable area by suppressing the unwanted terms. The reason for these problems is that, in the conventional approaches, the measured intensity or its band-pass filtered version (i.e., ψ_0 is first spatially filtered) is subjected to Fresnel propagation, whereas, ideally, one would like to Fresnel propagate the exact object wave, provided that it can be somehow computed from the hologram. This is precisely the philosophy pursued in this paper. Our method relies on some

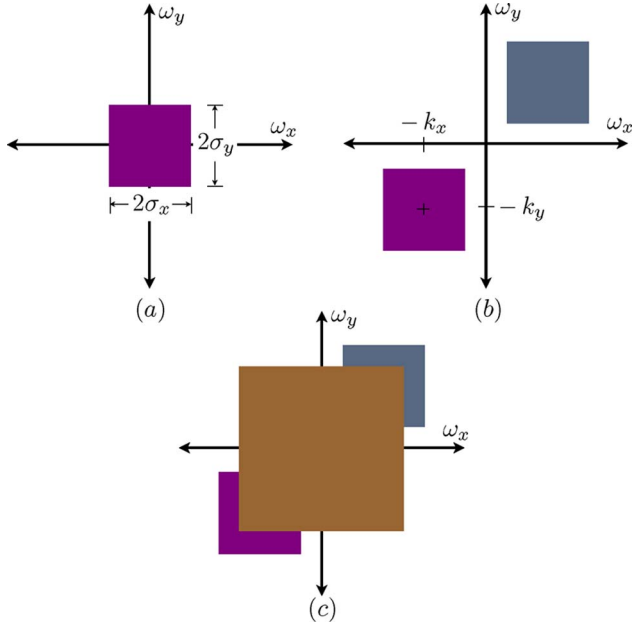


Fig. 3. (Color online) Spectral occupancy of (a) the object wave, (b) the modulated object wave, and (c) the hologram $i(\mathbf{x})$.

simple assumptions, which are easily fulfilled in practice. For the purpose of the theoretical developments, we work in the continuous domain. The implications for a discrete implementation are addressed separately in [18].

3. PROPOSED NONLINEAR RECONSTRUCTION TECHNIQUE

Consider the specific case of a plane wave reference, i.e., $r(\mathbf{x}) = A \exp(-i\langle \mathbf{k}, \mathbf{x} \rangle)$, where A is the complex amplitude. Corresponding to this choice, (1) reduces to

$$i(\mathbf{x}) = |A \exp(-i\langle \mathbf{k}, \mathbf{x} \rangle) + o(\mathbf{x})|^2 = |A|^2 \left| 1 + \underbrace{\frac{1}{A} \exp(i\langle \mathbf{k}, \mathbf{x} \rangle) o(\mathbf{x})}_{\tilde{o}(\mathbf{x}) = \frac{o(\mathbf{x})}{r(\mathbf{x})}} \right|^2. \tag{4}$$

Note that multiplication by $\exp(i\langle \mathbf{k}, \mathbf{x} \rangle)$ corresponds to a complex modulation of the object wave; the effect in the frequency domain is a translation of the spectrum of $o(\mathbf{x})$ to the location $-\mathbf{k}$. This is the well-known *modulation property* of the Fourier transform and plays a vital role in the subsequent developments. This property is illustrated in Figs. 3(a) and 3(b), where we have considered a 2D band-limited function. Consider the 2D Fourier transform of $i(\mathbf{x})$:

$$\mathcal{F}\{i\}(\boldsymbol{\omega}) = |A|^2 \{ \delta(\boldsymbol{\omega}) + \mathcal{F}\{o\}(\boldsymbol{\omega} + \mathbf{k}) + \mathcal{F}\{o\}(-\boldsymbol{\omega} - \mathbf{k}) + q(\boldsymbol{\omega}) \}, \tag{5}$$

where $q(\boldsymbol{\omega})$ denotes the 2D autocorrelation of $\mathcal{F}\{o\}(\boldsymbol{\omega})$. In the special case where $\mathcal{F}\{o\}(\boldsymbol{\omega})$ has a compact support $[-\sigma_x, \sigma_x] \times [-\sigma_y, \sigma_y]$, the autocorrelation also has compact support $[-2\sigma_x, 2\sigma_x] \times [-2\sigma_y, 2\sigma_y]$. The spectral occupancy of the various terms in (5) is shown in Fig. 3(c).

We next present the method to isolate the complex object wave and to suppress the zero-order. The method is based on the logarithm operator, which is employed to deconvolve the object wave from its twin image. This key result is presented

in the form of the following theorem. The proof is constructive and leads to the reconstruction method.

Theorem 1. If $\tilde{o} \in L^2(\mathbb{R} \times \mathbb{R})$ has a Fourier transform $\mathcal{F}\{\tilde{o}\}$ that is identically zero outside $[0, +\infty) \times [0, +\infty)$ and $|\tilde{o}| \leq \epsilon < 1$, then $|1 + \tilde{o}(\mathbf{x})|^2$ specifies $\tilde{o}(\mathbf{x})$ almost everywhere.

Proof. To prove the theorem, we first need the following lemmas.

Lemma 1. If $\tilde{o} \in L^2(\mathbb{R} \times \mathbb{R})$ has a Fourier transform $\mathcal{F}\{\tilde{o}\}$ that vanishes outside $[0, +\infty) \times [0, +\infty)$ and $|\tilde{o}| \leq \epsilon < 1$, then $\mathcal{F}\{\log(1 + \tilde{o})\}(\boldsymbol{\omega})$ is also identically zero outside $[0, +\infty) \times [0, +\infty)$ almost everywhere.

Proof. Since $|\tilde{o}| \leq \epsilon < 1$, we invoke the Taylor series expansion for $\log(1 + \tilde{o}(\mathbf{x}))$:

$$\log(1 + \tilde{o}(\mathbf{x})) = \sum_{n=1}^{\infty} \frac{(-1)^{n-1}}{n} \tilde{o}^n(\mathbf{x}). \tag{6}$$

Applying the Fourier transform operator \mathcal{F} on both sides of (6), we get that

$$\mathcal{F}\{\log(1 + \tilde{o})\}(\boldsymbol{\omega}) = \sum_{n=1}^{\infty} \frac{(-1)^{n-1}}{n} \mathcal{F}\{\tilde{o}^n\}(\boldsymbol{\omega}). \tag{7}$$

Recall that the Fourier transform of a product of n functions is the n -fold convolution of the Fourier transforms of the corresponding functions. Stated symbolically,

$$\mathcal{F}\{\tilde{o}^n\}(\boldsymbol{\omega}) = \underbrace{(\mathcal{F}\{\tilde{o}\} * \mathcal{F}\{\tilde{o}\} * \mathcal{F}\{\tilde{o}\} * \dots * \mathcal{F}\{\tilde{o}\})}_{n \text{ times}}(\boldsymbol{\omega}). \tag{8}$$

Since $\mathcal{F}\{\tilde{o}\}$ vanishes outside $[0, +\infty) \times [0, +\infty)$, the right-hand side of (8) also vanishes outside $[0, +\infty) \times [0, +\infty)$ almost everywhere. This property carries over to the right-hand side of (7).

Lemma 2. If $\tilde{o} \in L^2(\mathbb{R} \times \mathbb{R})$ and $\mathcal{F}\{\tilde{o}\}$ vanishes outside $[0, +\infty) \times [0, +\infty)$ and $|\tilde{o}| \leq \epsilon < 1$, then $\mathcal{F}\{\log(1 + \tilde{o}^*)\}(\boldsymbol{\omega})$ also vanishes outside $(-\infty, 0] \times (-\infty, 0]$ almost everywhere.

Proof. The proof is similar to that of lemma 1.

We now continue with the proof of theorem 1. Consider the factorization

$$\log |1 + \tilde{o}|^2 = \log(1 + \tilde{o}) + \log(1 + \tilde{o}^*). \tag{9}$$

Applying the Fourier transform on both sides gives rise to a new function, popularly known as the *cepstrum* [22,23], which we shall denote by $c(\boldsymbol{\omega})$:

$$\begin{aligned} c(\boldsymbol{\omega}) &= \mathcal{F}\{\log |1 + \tilde{o}|^2\}(\boldsymbol{\omega}) \\ &= \mathcal{F}\{\log(1 + \tilde{o})\}(\boldsymbol{\omega}) + \mathcal{F}\{\log(1 + \tilde{o}^*)\}(\boldsymbol{\omega}). \end{aligned} \tag{10}$$

By applying lemmas 1 and 2, it follows that the functions $\mathcal{F}\{\log(1 + \tilde{o})\}(\boldsymbol{\omega})$ and $\mathcal{F}\{\log(1 + \tilde{o}^*)\}(\boldsymbol{\omega})$ have nonoverlapping support. By retaining the region corresponding to the support of $\mathcal{F}\{\tilde{o}\}$, we have that

$$\mathcal{F}\{\log(1 + \tilde{o})\}(\boldsymbol{\omega}) = \mathcal{F}\{\log |1 + \tilde{o}|^2\}(\boldsymbol{\omega}) \cdot \mathbf{1}_{[0, +\infty) \times [0, +\infty)}, \tag{11}$$

where $\mathbf{1}_{[0, +\infty) \times [0, +\infty)}$ is the associated indicator function for selecting the first quadrant. Applying the inverse Fourier transform on both sides of (11), we have that

$$\begin{aligned} \log(1 + \tilde{o}(\mathbf{x})) &= \mathcal{F}^{-1}\{\mathcal{F}\{\log |1 + \tilde{o}|^2\} \cdot \mathbf{1}_{[0, +\infty) \times [0, +\infty)}\}(\mathbf{x}), \Rightarrow \tilde{o}(\mathbf{x}) \\ &= \exp(\mathcal{F}^{-1}\{\mathcal{F}\{\log |1 + \tilde{o}|^2\} \cdot \mathbf{1}_{[0, +\infty) \times [0, +\infty)}\})(\mathbf{x}) - 1. \end{aligned} \tag{12}$$

Equation (12) summarizes the technique for complex object-wave reconstruction. The conditions on the support of $\mathcal{F}\{\tilde{o}\}$ and on its magnitude can be realized in practice by suitably selecting the design parameters A , k_x , and k_y . The above framework also includes the special case where a phase factor $\exp(i\phi(x))$ is common to both the object and reference waves, since it does not affect the intensity of the hologram.

4. EXACT RECONSTRUCTION AND HOMOMORPHIC SIGNAL PROCESSING

The proof of theorem 1 involves the logarithm and the exponential, which are nonlinear in the conventional sense but which satisfy a generalized principle of superposition. The principle forms the basis of homomorphic signal processing. To explain further, we need to introduce a few definitions related to the cepstrum, which is of central importance in homomorphic signal processing. For a detailed treatment of cepstrum, the reader is referred to [24]. Our formulation is in the continuous-space and frequency domains, whereas the often-used one is a discrete-space, discrete/continuous-frequency domain formulation. We shall also confine our discussion to homomorphic operators specifically in the context of convolution. For a discussion on generalized operators, the reader is referred to [24].

A. Definition of Cepstrum

Let $f(x) \in L^2(\mathbb{R} \times \mathbb{R})$. The two-dimensional complex cepstrum of $f(x)$ is defined as

$$c_f(x) = \mathcal{F}^{-1}\{\log \mathcal{F}\{f\}\}(x). \tag{13}$$

The function $c_f(x)$ exists and has finite energy if $\log \mathcal{F}\{f\}(\omega) \in L^2(\mathbb{R} \times \mathbb{R})$. The real cepstrum is defined as the inverse Fourier transform of $\log |\mathcal{F}\{f\}|(\omega)$, i.e.,

$$c_r^f(x) = \mathcal{F}^{-1}\{\log |\mathcal{F}\{f\}|\}(x). \tag{14}$$

B. Homomorphic Operators

Consider an operator T that maps $f_1(x)$ and $f_2(x)$ into $T\{f_1\}(x)$ and $T\{f_2\}(x)$, respectively. Let T satisfy the generalized principle of superposition:

$$T\{f_1 * f_2\}(x) = T\{f_1\} * T\{f_2\}(x) \text{ (linearity)}, \tag{15}$$

$$T\{c \cdot f_1\}(x) = c \cdot T\{f_1\}(x) \text{ (scaling property)}, \tag{16}$$

where c is a scalar. T is said to be homomorphic with convolution as both input and output operation, and is denoted by $T\{*,*\}$. A homomorphic system $T\{*,*\}$ can be decomposed as a cascade of three homomorphic systems [24]: $D\{*,*\}$, $L\{+,*\}$, and $D^{-1}\{+,*\}$ [cf. Fig. 4]. Such a representation is referred to as the canonical decomposition of T . The operator $D\{*,*\}$ is referred to as the characteristic system associated with the input operation $*$; $D^{-1}\{+,*\}$ is the *inverse characteristic system* associated with the output operation $*$; and $L\{+,*\}$ is a linear system in the usual sense, i.e., it satisfies the classical principle of superposition. Block diagrams of the characteristic system and its inverse are shown in Fig. 5.

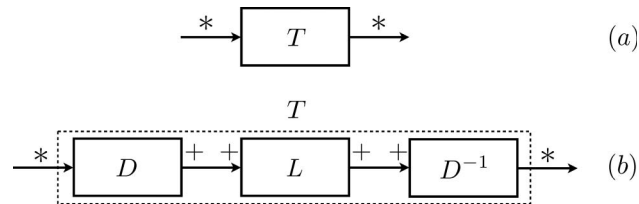


Fig. 4. (a) Homomorphic system with convolution operation at the input as well as at the output, (b) its canonical representation.

C. Nonlinear Reconstruction Technique and Homomorphic Equivalence

We next show that the proposed nonlinear reconstruction technique (NRT) is a homomorphic signal processing technique. To proceed, consider the hologram $i(x) = |1 + \tilde{o}(x)|^2$, which is the product of $(1 + \tilde{o}(x))$ and $(1 + \tilde{o}^*(x))$. Since the Fourier transform converts products to convolutions and vice versa, we have that $\mathcal{F}\{i\}(\omega) = \mathcal{F}\{(1 + \tilde{o})\}(\omega) * \mathcal{F}\{(1 + \tilde{o}^*)\}(\omega)$, that is, the spectra of the object wave and its conjugate are convolved. With reference to Fig. 5, let $\hat{f}(\omega) = \mathcal{F}\{(1 + \tilde{o})\}(\omega) * \mathcal{F}\{(1 + \tilde{o}^*)\}(\omega)$. Considering the transformations given in Figs. 4 and 5, we have the following:

$D\{*,*\}$:

1. Inverse Fourier transformation: $\hat{f}(\omega) \rightarrow i(x) = |1 + \tilde{o}(x)|^2$, which is the hologram;
2. logarithm: $i(x) \rightarrow \log i(x)$; and
3. Fourier transformation: $\log i(x) \rightarrow c(\omega) = \mathcal{F}\{\log i\}(\omega)$.

$L\{+,*\}$:

1. Selection of the first quadrant: $c^+(\omega) = c(\omega) \cdot \mathbf{1}_{[0,+\infty) \times [0,+\infty)}$. The operator $L\{+,*\}$ is referred to as *liftering* in homomorphic signal processing literature.

$D^{-1}\{+,*\}$:

1. Inverse Fourier transformation: $c^+(\omega) \rightarrow C^+(x) = \mathcal{F}^{-1}\{c^+\}(x)$;
2. exponentiation: $C^+(x) \rightarrow \exp(C^+(x)) = 1 + \tilde{o}(x)$; and
3. Fourier transformation: $1 + \tilde{o}(x) \rightarrow \mathcal{F}\{1 + \tilde{o}\}(\omega)$.

Since the hologram is available in the spatial domain, we have the output of step 1 of $D\{*,*\}$ directly to start with. Since the complex wave is required in the spatial domain, we stop with step 2 of $D^{-1}\{+,*\}$ in NRT. Therefore, effectively, NRT starts with step 2 of $D\{*,*\}$ and stops with step 2 of $D^{-1}\{+,*\}$.

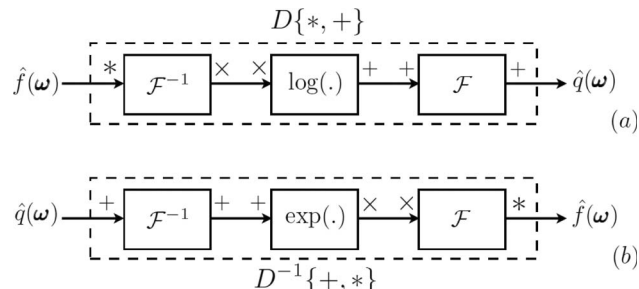


Fig. 5. (a) Characteristic system $D\{*,*\}$ for convolution, (b) its inverse $D^{-1}\{+,*\}$.

From the above correspondence, we infer that the reconstruction technique embedded in theorem 1 is equivalent to homomorphic deconvolution. More specifically, the spectrum of the object wave is deconvolved from that of its conjugate, which would otherwise give rise to the twin image and zero-order. The key property aiding deconvolution is that the cepstra of the object wave and its complex conjugate have disjoint supports (cf. lemmas 1 and 2). As a result of applying the proposed reconstruction technique, the complex object wave is obtained, which is then Fresnel propagated to perform reconstruction.

The above analysis transposes the problem of zero-order suppression and complex object-wave recovery to one of deconvolution. The implication is that alternative deconvolution algorithms may also potentially solve the zero-order problem provided that they are appropriately designed.

5. PERFORMANCE VALIDATION

In this section, we present results on simulated data as well as experimental data to validate the accuracy of the reconstruction technique.

A. Simulation Results

We designed a phantom representing cell culture in amplitude and phase [cf. Fig. 6(a)]. The amplitude profile is chosen to create large spatial frequencies. Further, some phase noise is added to simulate the actual measurement conditions. The phase noise is chosen to follow a uniform distribution over $[-\frac{\pi}{25}, \frac{\pi}{25}]$ radians. The simulation parameters are chosen so that the two conditions required by the proposed reconstruction technique are satisfied. The reference intensity is chosen to be three times stronger than the constant background of the object; the average intensity ratio in the image is 4.3, and the minimum ratio is 1.45.

The other parameters are taken as approximately identical to the experimental ones of Section 5.B ($\lambda = 680$ nm, $\Delta x = \Delta y = 6.45$ μ m). The simulated hologram is then created by applying the following steps to the synthesized complex wave field:

- A lowpass filter with a circular spectral support is applied to the complex wave field. The diameter of the circle is chosen as 117 pixels, corresponding to an imaging system

with a magnification $M = 5\times$ and a numerical aperture $NA = 0.12$.

- The low-pass filtered complex wave field is digitally propagated to the Fresnel zone, according to (3), with a propagation distance $d = 4.9$ cm.

- The simulated hologram is then obtained by calculating the coherent addition of the propagated complex wave field with a tilted reference plane wave and by taking the modulus, according to (1). The angle θ between the propagation vectors of the two waves is chosen as 2° , so as to ensure that the desired imaging order and the twin image are separated, but they overlap with the zero-order.

- Finally, the hologram is saved as an 8 bit image, to take quantization also into account.

Since the object simulated contains more informative phase than amplitude, we focus on the accuracy of phase reconstruction. The reconstruction results are shown in Fig. 6, where the phase of the original object used for generating the hologram [Fig. 6(a)] is compared with that given by the standard Fourier method [Fig. 6(b)] and the proposed technique [Fig. 6(c)]. We note that there are strong artifacts in the standard Fourier reconstruction, which are primarily due to the zero-order disturbance. The NRT suppresses those artifacts and retrieves the phase information accurately. To quantify the accuracy of reconstruction, we calculated the differences between the various reconstructions and the ideal ground truth, which is generated by using a zero-order-free hologram computed as $i_{\text{ideal}}(\mathbf{x}) = i(\mathbf{x}) - |r(\mathbf{x})|^2 - |\rho(\mathbf{x})|^2$, where both $|r(\mathbf{x})|^2$ and $|\rho(\mathbf{x})|^2$ are known in this simulation. The phase differences between the ideal reconstruction and the phase images of Fig. 6 are presented in Fig. 7. In the standard reconstruction [Fig. 7(a)], strong phase variations of the order of $\frac{\pi}{4}$ were found to occur. Such variations are suppressed by the NRT [cf. Fig. 7(b)]; indeed, no strong artifacts are visible even when the signal dynamic range is zoomed in by a factor of 5. One can identify a mild pattern in the reconstruction of Fig. 7(b), which is due to the harmonics generated by the nonlinear operations. The intensities of the harmonics can be further reduced by increasing the intensity ratio between the reference and object waves. In this experiment, the minimum intensity ratio is 1.45, which is slightly above unity.

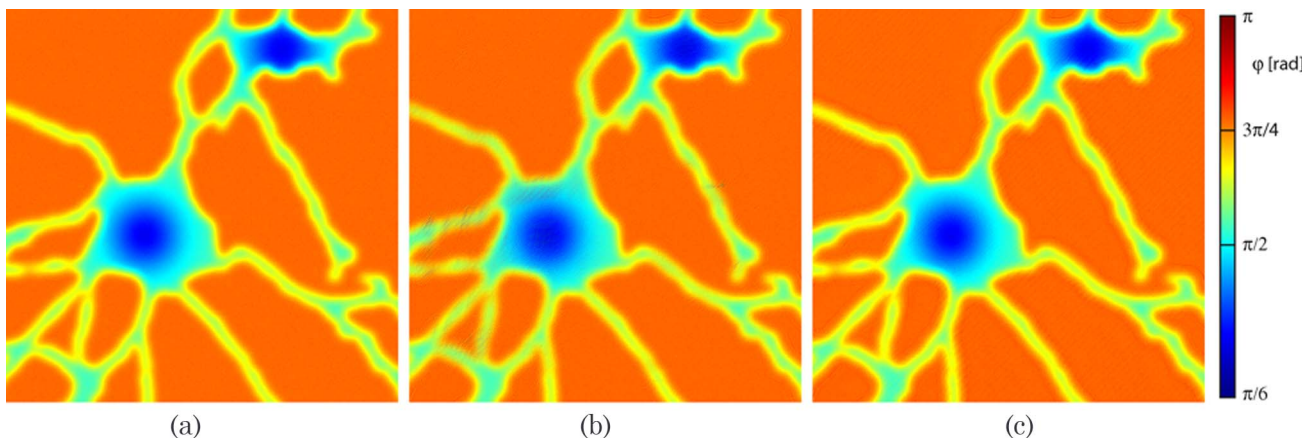


Fig. 6. (Color online) Phase of the phantom used in simulations. (a) Ground truth phase used in hologram simulation, (b) phase obtained by the standard Fourier method, and (c) phase of the nonlinear reconstruction.

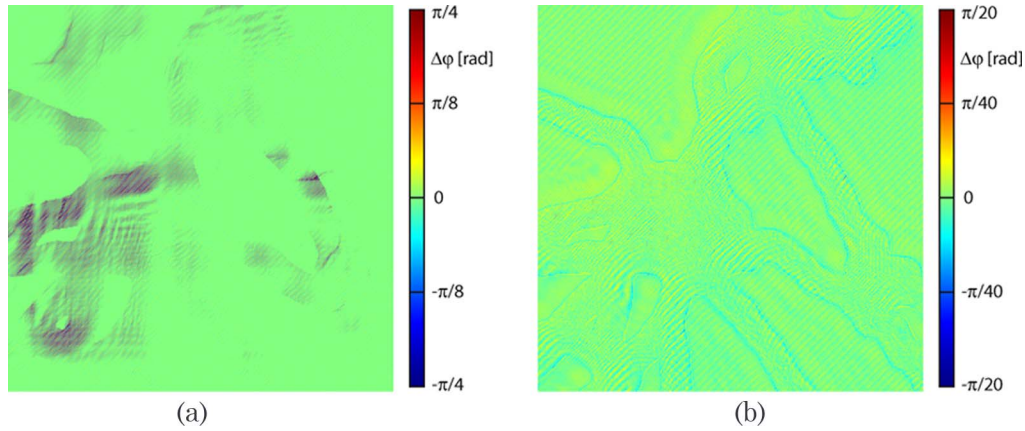


Fig. 7. (Color online) Phase difference between the ground truth and that obtained by (a) the standard Fourier reconstruction, and (b) the nonlinear reconstruction technique.

B. Experiments on Real Data

To experimentally demonstrate the capability of the NRT, we measured a solution of yew pollens with a standard transmission digital holographic microscope [11]. The specimen is illuminated with a laser diode ($\lambda = 680$ nm), and the light is collected with a $5\times$ microscope objective ($\text{NA} = 0.12$). The hologram is recorded by a CCD ($\Delta x = 6.45$ μm) with a shutter time of the order of a few milliseconds. To ensure that the reference intensity is higher than that of the object, the intensity ratio of the beams is controlled through polarizing optical elements. In our experiments, the average ratio of the reference-wave intensity to that of the object wave is measured to be 13.3, and the minimum ratio in the field of view is 4.29. The differences in the intensity ratios across pixels is due to the fact that the specimen is not uniformly diffractive. Components such as cell walls lead to strong diffraction and result in spatially different intensity ratios. The object wave field is reconstructed by first filtering the relevant quadrant of the Fourier spectrum [cf. Fig. 8] and then demodulating the signal to suppress the linear phase term introduced by the off-axis configuration employed during acquisition. Finally, the wave field is Fresnel propagated and the best focus is achieved at the recording distance of $d = 4.9$ cm. The reconstructions obtained are shown in Fig. 9, for the standard linear Fourier filtering [cf. Figs. 9(a) and 9(c)] and the proposed nonlinear technique [cf. Figs. 9(b) and 9(d)]. The phase maps are unwrapped in order to suppress the phase jumps. The dynamic range of the phase in the case of Figs. 9(c) and 9(d) is 6.61 radians. Using a small magnification factor ensures that spectral overlap occurs between the zero-order and the imaging terms. Since one full quadrant of the hologram is employed in reconstruction, a part of the zero-order is contained in the reconstructed wave field in the case of linear reconstruction. This term can be readily identified as a high-frequency oscillation in both the amplitude [cf. Fig. 9(a)] and phase images [cf. Fig. 9(c)]. The zero-order appears as a high-frequency oscillation because of the demodulation step involved in the process of hologram reconstruction. The NRT, on the other hand, suppresses the zero-order artifacts [cf. Figs. 9(b) and 9(d)]. The reconstructed amplitude shown in Fig. 9(b) has a nearly constant background, which corresponds to the solution in which the specimen is contained. The oscillating components in the phase image [cf. Fig. 9(d)] are also much reduced. In addition, the contrast of the phase image is better than that of the

standard linear reconstruction. The improvement in quality is due to the suppression of the nearly constant phase component contributed by the zero-order. The parameters of the experimental setup employed in this paper are slightly different from those in [18]. A $5\times$ MO ($\text{NA} = 0.12$) is used here whereas a $10\times$ MO ($\text{NA} = 0.25$) was used in [18]. Measurements with lower numerical apertures result in more overlap between various orders if one wants to keep the full resolution provided by the optical system. As the results in Fig. 9 show, the NRT offers good reconstruction performance and results in high-contrast phase images even for low NA measurements.

6. A HILBERT TRANSFORM PERSPECTIVE

In this section, we establish a connection between the proposed reconstruction technique and one particular extension of the Hilbert transform in higher-dimensional spaces developed by Hahn [25,26].

A. Preliminaries

The Hilbert transform of a real-valued square-integrable 1D function $h(x)$, denoted by $\mathcal{H}\{h\}(x)$ is best described in the Fourier domain as

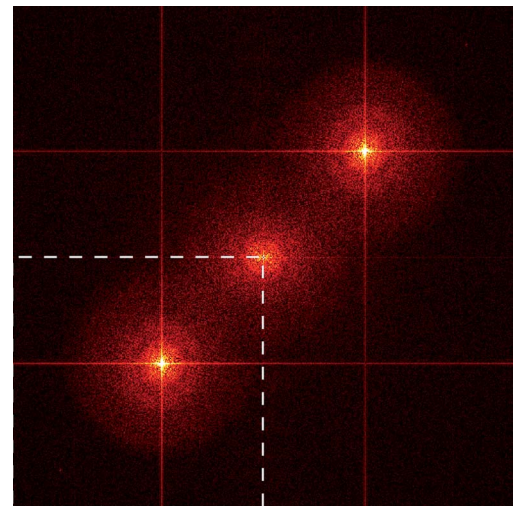


Fig. 8. (Color online) Fourier transform of a hologram of yew pollens. The dashed zone highlights the filtered region used in the reconstructions of Fig. 9.

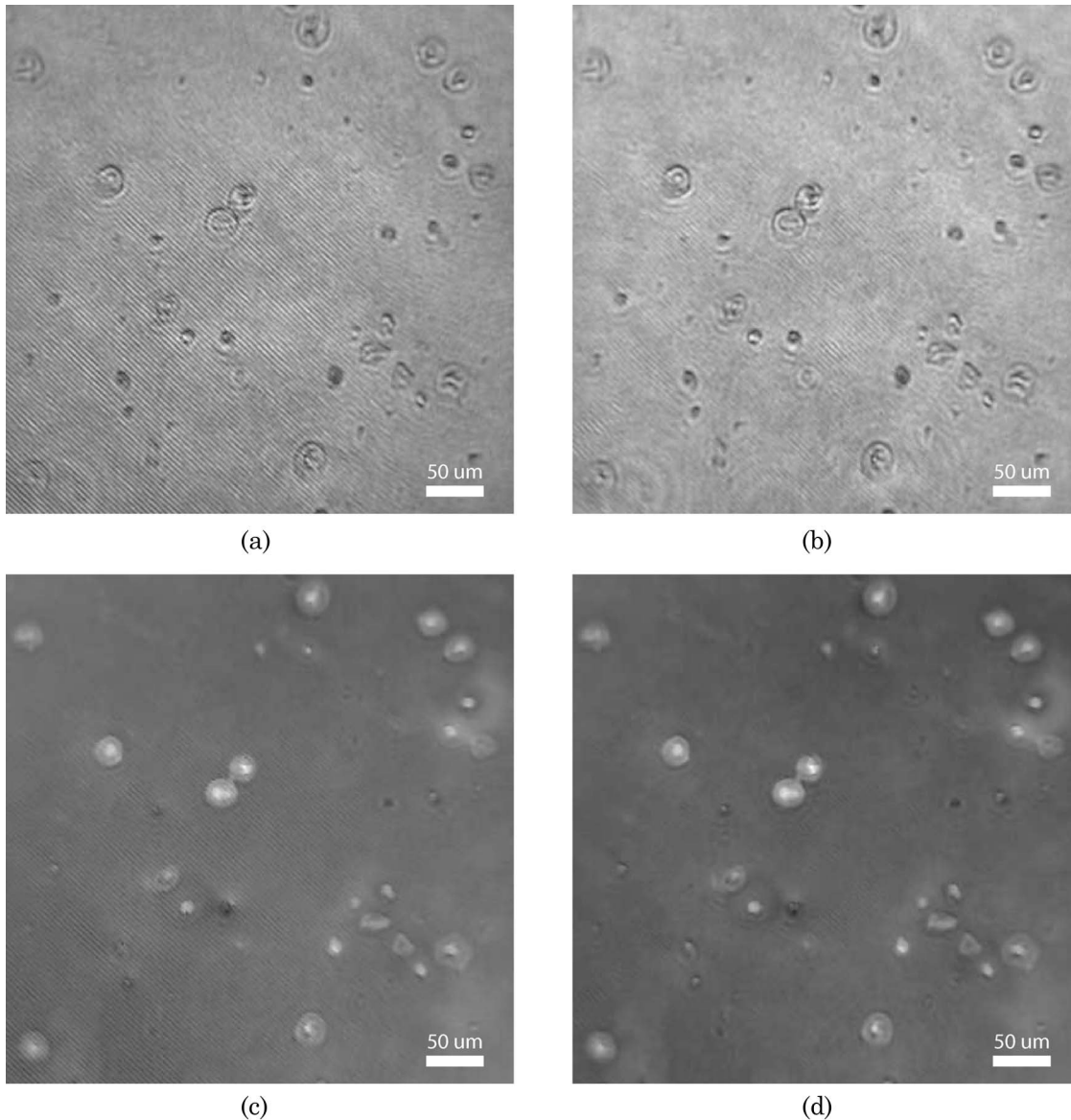


Fig. 9. Specimen: solution of yew pollens. The hologram is reconstructed with (a), (c) standard Fourier filtering and (b), (d) with the proposed nonlinear technique, where amplitude (a), (b) and phase (c), (d) images are shown.

$$\mathcal{H}\{h\}(x) \xrightarrow{\mathcal{F}} -i \operatorname{sign}(\omega) \mathcal{F}\{h\}(\omega), \quad (17)$$

where $\operatorname{sign}(\omega)$ is the signum function. $\mathcal{H}\{h\}(x)$ has the same magnitude spectrum as $h(x)$ but its phase spectrum is offset by $\frac{\pi}{2}$ for negative frequencies and $-\frac{\pi}{2}$ for positive frequencies. The 1D analytic signal is defined as $a_h(x) = h(x) + i \mathcal{H}\{h\}(x)$; its Fourier transform is

$$\mathcal{F}\{a_h\}(\omega) = (1 + \operatorname{sign}(\omega)) \mathcal{F}\{h\}(\omega). \quad (18)$$

The frequency domain specification of the operator that relates the function to its analytic counterpart is $(1 + \operatorname{sign}(\omega)) = 2 \cdot \mathbf{1}_{[0, +\infty)}(\omega)$. Computing the analytic signal corresponds to retaining only the positive half of the spectrum. Based on this observation, Hahn [25] extended the definition of the Hilbert transform to 2D signals in such a way that the complex signal has a nonzero spectrum in the positive quadrant. In the general multidimensional case, the spectrum of the complex signal is nonzero in the positive orthant. Hahn's generalization

is based on a separable extension of the Hilbert transform. The corresponding 2D complex signal (counterpart of the 1D analytic signal) is defined in the Fourier domain as

$$\begin{aligned} \mathcal{F}\{a_h\}(\omega) &= (1 + \operatorname{sign}(\omega_x))(1 + \operatorname{sign}(\omega_y)) \mathcal{F}\{h\}(\omega) \\ &= (1 + \operatorname{sign}(\omega_x) + \operatorname{sign}(\omega_y) \\ &\quad + \operatorname{sign}(\omega_x)\operatorname{sign}(\omega_y)) \mathcal{F}\{h\}(\omega) \\ &= 4 \cdot \mathbf{1}_{[0, +\infty) \times [0, +\infty)}(\omega) \mathcal{F}\{h\}(\omega), \end{aligned} \quad (19)$$

which is nonzero only in the first quadrant. The corresponding complex signal $a_h(x)$ is said to possess a *single-quadrant spectrum*, a term coined by Hahn. By splitting the operator on the right-hand side of (19), we have that

$$\begin{aligned} \mathcal{F}\{a_h\}(\omega) &= \mathcal{F}\{h\}(\omega) + i\{-i \operatorname{sign}(\omega_x) - i \operatorname{sign}(\omega_y) \\ &\quad - i \operatorname{sign}(\omega_x)\operatorname{sign}(\omega_y)\} \mathcal{F}\{h\}(\omega), \end{aligned} \quad (20)$$

where $-i \operatorname{sign}(\omega_x)$, and $-i \operatorname{sign}(\omega_y)$ are the frequency responses associated with the Hilbert transform operators

acting along x and y directions, respectively. The corresponding operators are denoted by \mathcal{H}_x and \mathcal{H}_y , respectively, and are referred to as partial Hilbert transform operators. The function $-i \operatorname{sign}(\omega_x)\operatorname{sign}(\omega_y)$ is the frequency response associated with the total Hilbert transform operator denoted by \mathcal{H}_{xy} . These operators are skew-adjoint; i.e., $\mathcal{H}_x \circ \mathcal{H}_x = -\mathcal{I}$, $\mathcal{H}_y \circ \mathcal{H}_y = -\mathcal{I}$, and $\mathcal{H}_{xy} \circ \mathcal{H}_{xy} = -\mathcal{I}$, where \mathcal{I} denotes the identity operator and \circ is the symbol for the composition of operators. These properties can be readily proved by working in the Fourier domain.

B. Partial Hilbert Transform Relations

Consider the following representation for $a_h(\mathbf{x})$:

$$a_h(\mathbf{x}) = \operatorname{Re}\{a_h\}(\mathbf{x}) + i \operatorname{Im}\{a_h\}(\mathbf{x}), \quad (21)$$

where $\operatorname{Re}\{\cdot\}$ and $\operatorname{Im}\{\cdot\}$ correspond to the real and imaginary parts, respectively, of the argument. Based on the definition of $a_h(\mathbf{x})$, we have that

$$\operatorname{Re}\{a_h\}(\mathbf{x}) = h(\mathbf{x}) - (\mathcal{H}_x \circ \mathcal{H}_y)h(\mathbf{x}), \quad (22)$$

$$\operatorname{Im}\{a_h\}(\mathbf{x}) = \mathcal{H}_x h(\mathbf{x}) + \mathcal{H}_y h(\mathbf{x}). \quad (23)$$

It can be shown that the real and imaginary parts are orthogonal to each other, i.e., their inner product is zero:

$$\langle \operatorname{Re}\{a_h\}, \operatorname{Im}\{a_h\} \rangle_{L^2(\mathbb{R} \times \mathbb{R})} = 0. \quad (24)$$

In addition, there are primary Hilbert transform relations between the real and imaginary parts:

$$\mathcal{H}_x\{\operatorname{Re}\{a_h\}\}(\mathbf{x}) = \mathcal{H}_y\{\operatorname{Re}\{a_h\}\}(\mathbf{x}) = \operatorname{Im}\{a_h\}(\mathbf{x}). \quad (25)$$

From (25), we derive the pair of secondary relations:

$$\mathcal{H}_x\{\operatorname{Im}\{a_h\}\}(\mathbf{x}) = \mathcal{H}_y\{\operatorname{Im}\{a_h\}\}(\mathbf{x}) = -\operatorname{Re}\{a_h\}(\mathbf{x}). \quad (26)$$

The proofs for (24)–(26) can be given by invoking the spectral properties of the partial Hilbert transform operators. Although (25) and (26) follow from the definitions of the operators, it does not seem to have been explicitly remarked in the literature that such relations exist in the 2D case. In our view, these relations are the 2D counterpart of the well-known Hilbert integral equations, Titchmarsh theorem, or Dispersion relations in the 1D case [27,28], which state that if a finite-energy 1D function is analytic, then its real and imaginary parts form a Hilbert transform pair.

C. Relations Between Magnitude and Phase

Having listed some important properties of functions with a single-quadrant spectrum, we next establish the connection with the nonlinear reconstruction technique. Recall from (12) that

$$\log(1 + \tilde{o}(\mathbf{x})) = \mathcal{F}^{-1}\{\mathcal{F}\{\log|1 + \tilde{o}|^2\} \cdot \mathbf{1}_{[0,+\infty) \times [0,+\infty)}\}(\mathbf{x}), \quad (27)$$

which clearly shows that $\log(1 + \tilde{o})$ has a single-quadrant spectrum and is therefore complex. Therefore, its real and imaginary parts must obey the partial Hilbert transform rela-

tions stated in (25) and (26). Note, however, that $\log(1 + \tilde{o}(\mathbf{x}))$ can also be rewritten as

$$\log(1 + \tilde{o}(\mathbf{x})) = \log|1 + \tilde{o}(\mathbf{x})| + i\angle(1 + \tilde{o}(\mathbf{x})), \quad (28)$$

where \angle denotes the unwrapped phase angle of its argument; the real part is the log magnitude and the imaginary part is the phase. Thus, the partial Hilbert transform relations apply to the log magnitude and phase of the complex wave. Since the magnitude is the measured quantity, exploiting this relation amounts to retrieving the phase from the logarithm of the magnitude spectrum. Such a relation is known for a special class of causal signals in 1D known as minimum-phase signals. However, it does not seem to have been transposed to 2D or exploited for the special case of signals with single orthant spectra. This connection also places the new reconstruction technique in the general context of phase retrieval with a sound theoretical basis.

The above formalism also fits naturally into the framework of single-quadrant modulation proposed by Hahn [25]. In his paper, Hahn makes a concluding remark that applications of 2D or higher-dimensional modulation have to be found. As we have shown in this paper, single-quadrant modulation turns out to be the natural choice in digital holography, mainly from the point of view of zero-order free reconstruction. This type of modulation also has the added advantage of better preserving the spatial resolution of fringes.

7. CONCLUSIONS

We have laid the theoretical foundations for a new reconstruction technique for digital hologram reconstruction. We have shown that, under realistic conditions, it is possible to achieve exact complex-wave reconstruction by a combination of linear and nonlinear operations. As a result, the zero-order is suppressed. The operations involved satisfy the generalized principle of superposition, which forms the basis for homomorphic signal processing. By recognizing this equivalence, we have interpreted the reconstruction technique from the perspective of homomorphic deconvolution. We have also established connections with Hahn's multidimensional generalization of the Hilbert transform. The proposed theory naturally fits into Hahn's framework of single-quadrant modulation. This connection leads to new partial Hilbert transform relations between the logarithm of the measured magnitude and the unknown phase, thus implying that one can be computed from the other. It must be noted that, although Fresnel holography was considered in the development of the reconstruction technique and the experiments, the technique is not limited to this specific holographic modality. Since the technique deals with complex wave field recovery and is based on the fundamental equations of interference between two waves, it can be applied to any type of off-axis holography provided that the associated conditions are fulfilled. Throughout our analysis in this paper, we employed planar reference waves. Extending the results reported in this paper to the general case of nonplanar waves appears to be an interesting but nontrivial problem.

ACKNOWLEDGMENTS

C. S. Seelamantula was supported by the startup grant (14-0403-0012-01) from Indian Institute of Science, Bangalore, and the Department of Science and Technology—Intensive

Research in High Priority Areas (DSTO-943). N. Pavillon and C. Depeursinge were supported by the Swiss National Science Foundation (205320-120118). M. Unser was supported by the Centre for Biomedical Imaging of the Geneva-Lausanne universities and the Ecole polytechnique fédérale de Lausanne (EPFL) and the foundations Hasler, Leenards, and Louis-Jeantet.

REFERENCES

1. U. Schnars and W. P. O. Jüptner, "Digital recording and numerical reconstruction of holograms," *Meas. Sci. Technol.* **13**, R85–R101 (2002).
2. O. Coquoz, R. Conde, F. Taleblou, and C. Depeursinge, "Performance of endoscopic holography with a multicore optical fiber," *Appl. Opt.* **34**, 7186–7193 (1995).
3. U. Schnars, "Direct phase determination in hologram interferometry with use of digitally recorded holograms," *J. Opt. Soc. Am. A* **11**, 2011–2015 (1994).
4. B. Kemper and G. Von Bally, "Digital holographic microscopy for live cell applications and technical inspection," *Appl. Opt.* **47**, A52–A61 (2008).
5. P. Marquet, B. Rappaz, P. Magistretti, E. Cuche, Y. Emery, T. Colomb, and C. Depeursinge, "Digital holographic microscopy: a noninvasive contrast imaging technique allowing quantitative visualization of living cells with subwavelength axial accuracy," *Opt. Lett.* **30**, 468–470 (2005).
6. F. Dubois, N. Callens, C. Yourassowsky, M. Hoyos, P. Kurowski, and O. Monnom, "Digital holographic microscopy with reduced spatial coherence for three-dimensional particle flow analysis," *Appl. Opt.* **45**, 864–871 (2006).
7. W. Osten, T. Baumbach, and W. Jüptner, "Comparative digital holography," *Opt. Lett.* **27**, 1764–1766 (2002).
8. J. Kühn, F. Charrière, T. Colomb, E. Cuche, F. Montfort, Y. Emery, P. Marquet, and C. Depeursinge, "Axial sub-nanometer accuracy in digital holographic microscopy," *Meas. Sci. Technol.* **19**, 074007 (2008).
9. F. Montfort, Y. Emery, E. Solanas, E. Cuche, N. Aspert, P. Marquet, C. Joris, J. Kühn, and C. Depeursinge, "Surface roughness parameters measurements by Digital Holographic Microscopy (DHM)," in *Third International Symposium on Precision Mechanical Measurements* (SPIE, 2006), Vol. 6280 I, pp. 62800V-1–62800V-6.
10. F. Montfort, Y. Emery, F. Marquet, E. Cuche, N. Aspert, E. Solanas, A. Mehdaoui, A. Ionescu, and C. Depeursinge, "Process engineering and failure analysis of MEMS and MOEMS by digital holography microscopy (DHM)," in *International Symposium on MOEMS–MEMS 2007 Micro and Nanofabrication: Reliability, Packaging, Testing, and Characterization of MEMS/MOEMS VI*, A. L. Hartzell and R. Rameshuni (SPIE, 2007), Vol. 6463, pp. 64630G-1–64630G-7.
11. E. Cuche, P. Marquet, and C. Depeursinge, "Simultaneous amplitude-contrast and quantitative phase-contrast microscopy by numerical reconstruction of Fresnel off-axis holograms," *Appl. Opt.* **38**, 6994–7001 (1999).
12. I. Yamaguchi and T. Zhang, "Phase-shifting digital holography," *Opt. Lett.* **22**, 1268–1270 (1997).
13. E. N. Leith and J. Upatnieks, "Reconstructed wavefronts and communication theory," *J. Opt. Soc. Am.* **52**, 1123–1130 (1962).
14. M. Takeda, H. Ina, and S. Kobayashi, "Fourier-transform method of fringe-pattern analysis for computer-based topography and interferometry," *J. Opt. Soc. Am.* **72**, 156–160 (1982).
15. E. Cuche, P. Marquet, and C. Depeursinge, "Spatial filtering for zero-order and twin-image elimination in digital off-axis holography," *Appl. Opt.* **39**, 4070–4075 (2000).
16. T. M. Kreis and W. P. O. Jueptner, "Suppression of the dc term in digital holography," *Opt. Eng.* **36**, 2357–2360 (1997).
17. C. S. Seelamantula, N. Pavillon, C. Depeursinge, and M. Unser, "Zero-order-free image reconstruction in digital holographic microscopy," in *IEEE International Symposium on Biomedical Imaging: From Nano to Micro* (IEEE, 2009), pp. 201–204.
18. N. Pavillon, C. S. Seelamantula, J. Kühn, M. Unser, and C. Depeursinge, "Suppression of the zero-order in off-axis digital holography through nonlinear filtering," *Appl. Opt.* **48**, H186–H195 (2009).
19. J. R. Fienup, "Phase retrieval algorithms: a comparison," *Appl. Opt.* **21**, 2758–2769 (1982).
20. J. W. Goodman and R. W. Lawrence, "Digital image formation from electronically detected holograms," *Appl. Phys. Lett.* **11**, 77–79 (1967).
21. F. Montfort, F. Charrière, T. Colomb, E. Cuche, P. Marquet, and C. Depeursinge, "Purely numerical compensation for microscope objective phase curvature in digital holographic microscopy: influence of digital phase mask position," *J. Opt. Soc. Am. A* **23**, 2944–2953 (2006).
22. B. P. Bogert, M. J. R. Healy, and J. W. Tukey, "The frequency analysis of time series for echoes: cepstrum, pseudo-autocovariance, cross-cepstrum, and saphe cracking," in *Time Series Analysis*, M. Rosenblatt, ed. (Wiley, 1963), ch. 15, pp. 209–243.
23. J. Lim, *Two-Dimensional Signal and Image Processing* (Prentice-Hall, 1990).
24. A. V. Oppenheim and R. W. Schaffer, *Discrete Time Signal Processing*, 2nd ed. (Prentice Hall, 1999).
25. S. L. Hahn, "Multidimensional complex signals with single-orthant spectra," *Proc. IEEE* **80**, 1287–1300 (1992).
26. S. L. Hahn, *Hilbert Transforms in Signal Processing* (Artech House, 1996).
27. R. Bracewell, *The Fourier Transform and Its Applications*, 3rd ed. (McGraw-Hill, 1999).
28. A. Papoulis, *Signal Analysis* (McGraw-Hill, 1977).